Improved Photoactivity Of NiO/ZnO Nanorods Heterostructured Films Relying On Scaffold Surface Cleaning And NiO Deposition Time Optimization

Shanmugapriya Periyannan,[a, b] Laura Manceriu,*[a] Andreas Klein,[b] Wolfram Jaegermann,[b] Catherine Henrist,[a] and Rudi Cloots*[a]

Herein, a surface cleaning procedure involving vacuum anneal¬ing under oxygen was applied for cleaning the zinc oxide nanorod (ZNR) scaffold film's surface before nickel oxide (NiO) deposition for heterostructure formation. The scaffold proper¬ties (surface stoichiometry, defects fluctuation, Fermi level shift, carrier concentration) were studied as a function of the vacuum level and the NiO deposition time and correlated to the NiO/ ZNR interface (charge transfer resistance, band bending) and photo-response properties. The surface cleaning under a higher vacuum enabled the adsorbate and surface oxygen vacancy passivation but also influenced the surface doping. Our best
performing NiO/ZNR interface in terms of photocatalytic efficiency was composed of a high-vacuum-cleaned (0.5 Pa) ZNR scaffold and 40 s sputter deposited NiO layer which was post-annealed. The high photocatalytic efficiency could be correlated with a maximized near-band edge emission, effective band bending, low charge transfer resistance (as proven by photoelectrochemical impedance measurements), and opti¬mum light harvesting (maximized photocurrent density). The optimized NiO/ZNR showed about 1.5 times increase in photoresponse and improved photodegradation efficiency compared to the ZNR scaffold
Keywords: Interfaces · nanostructures · photocatalysis · photoelectron spectroscopy · surface cleaning · thin films

Introduction

Understanding the relationship between surface/interface properties and material performance is a complicated matter that needs to be taken into account when designing and optimizing any photocatalytic system.[1,2] Metal oxide semiconductors are extensively investigated as photocatalysts since the discovery of the water-splitting process by Fujishima and Honda in 1972.[3] However, they are generally known to have defects such as oxygen or cation vacancies which are highly reactive and capable of influencing the material's electrical and optical properties,[4,5] but also the photocatalytic process. The presence of vacancies results in co-ordinately unsaturated surfaces that attract impurities in the atmosphere (water, carbon dioxide), forming dangling bonds that act as charge trapping centers[6] and hinder the surface catalytic reactions. In addition, the vacancy type (metal or oxygen, in the case of metal oxides) and location within the material (shallow/surface
or deep/bulk) can impact the surface reactivity in catalytic reactions. The photocatalytic process is based on near-surface reactions and uses surface-localized charge carriers for adsorbing chemical species. Charges trapped at deep levels cannot participate in such reactions.[7,8] For bare/scaffold material surface defects might enhance the photocatalytic activity, but their presence while forming an interface with another material is not desirable as they promote the photo-generated charge recombination. When the charge accumulates on both sides as an effect of deficient transfer kinetics, the band bending is weakened and a drop in the photocatalytic performance can be observed.

Over the years, both experimental and computational approaches have been developed to study the surface-related properties and reactions of photocatalytic materials.[8,9] Contradictory opinions on the role of oxygen vacancies in the catalytic processes have been reported.[10–12] Previous works on reference TiO_2 n-type photocatalysts have revealed that the photo- catalytic activity can be enhanced by increasing the concentration ratio of surface defects to bulk defects by annealing[13,14] or by doping.[15,16]

Likewise, choosing the right morphology plays a crucial role in structural stability and photocatalytic activity, influencing the preferential charge localization and transfer rate. Remarkable catalytic activity and short activity time were observed for the 1D nanostructures,[17] despite their lower specific surface compared to flower-like or

nanosphere morphologies, owing to the facile pollutant access to the active sites. In addition, 1D nanomaterials have an increased light harvesting capability and direct electron pathway allowing efficient charge transport.[18–21] The surface charge distribution is very much dependent on material structure.[22] Mao *et al.*[23] revealed through photo-luminescence analysis that the ZnO with nanosphere morphology have a higher concentration of deep charge trapping centers as opposed to nano-disk or flowerlike structures. As- prepared ZnO nanorods were shown to possess high photo- catalytic activity due to a high percentage of (001) facets which are highly polar (the Zn terminated (100) facet is positive whereas the O terminated one is negative) enabling charge separation on the crystal facets[24] and HO preferential adsorption on the positive one.[25]

Despite the complexity involved in studying these effects, these inceptive studies lead to the same conclusion: a fine control over the surface charge and defects is essential for predictable photocatalytic activity, especially for n-type photocatalysts.

ZnO is an attractive metal oxide semiconductor for numerous applications[26] and its surfaces and interfaces were systematically studied since the first time published five decades ago by G. Heiland.[27] Since then, most often studies were carried out on defect-free single-crystal ZnO related to electronic or optical-oriented applications.[28] Oxygen vacancies were often attributed to the n-type conductivity in ZnO and govern the optical, semiconducting, and catalytic properties.[29]

The ZnO oxygen vacancy content can easily be modified by annealing in O_2-rich or O_2-poor atmospheres.[17–19] The formation (through annealing in presence of hydrogen/argon/ nitrogen)[30,31] or passivation (through annealing in presence of oxygen)[30–32] of oxygen vacancies can influence the catalytic reaction, due to the different band bending induced at the surface (Figure 1). Moreover, the oxygen vacancies filling/ creation process was observed for different particle sizes or shapes (nanospheres, nanocubes, nanorods, nanotubes, nanoflowers) in different types of n-type metal oxides (MgO, ZnO, TiO_2).[29–32]

For example, Tu *et al.*[29] demonstrated through X-ray photoelectron spectroscopy (XPS), Photoluminescence (PL), and Mott-Schottky (MS) analysis that by annealing in an N_2 atmosphere, the sol-gel deposited ZnO nanorod films increased the oxygen vacancy content, whereas the opposite happened when annealing in O_2 atmosphere. Similarly, Chevalier-César *et al.*[32] followed the evolution of defects by PL analysis for hydrothermally grown ZnO nanorods deposited on Si substrates. The deep-level oxygen defects (yellow- and orange-red- coloured emission peaks) increased with growth time, whereas the oxygen interstitial content (green-coloured emission) was found to be almost constant for the as-deposited films. After post-annealing in the air at 400°C, the number of deep-level defects decreased thus lowering the green emission intensity. Further studies[33,34] also employed PL as the main characterization tool to analyze the defect levels in ZnO and noted the green emission reduction in the presence of oxygen. A blue shift was also noticed and attributed to the neutral oxygen vacancies ionization. Drouilly *et al.*[30] performed electron paramagnetic resonance (EPR) and PL analysis on defect-rich ZnO and found that the annealing atmosphere (O_2, N_2, vacuum, and $O_2 + N_2$) and the gas pressure modifies the oxygen vacancies concentration. Under oxygenated annealing, a competition between the formation and filling of vacancies occurs and the prevalence of any of these processes depends on the temperature and the oxygen partial pressure. In general, the filling of vacancies was observed when annealing in an oxygen rich atmosphere, while vacancy formation was observed in oxygenpoor conditions.

The enhancement in performance of the ZnO photo- catalytic systems is often correlated with the deep-level emission quenching or the increase in the surface emission,[35,36] and a handful of studies talk about the role of oxygen vacancies in the photocatalytic process.[10,37] However, the correlation of surface and interfacial defects with the photoelectrochemical properties was only recently initiated for powders and films.[38,39] Hence, for the first time, such correlations are explored for hydrothermally grown ZnO nanorods (ZNR) and corresponding NiO/ ZNR heterostructures as a function of the vacuum pressure during annealing and NiO deposition time.

In general, the metal oxide heterostructure formation and its improved performance with report to single material accounted for a convenient band bending, without much experimental proof of either the interface quality or the band energy[40–43] quantification. For example, Zeng *et al.*[44] reported a 2-fold improvement in photocurrent density for $Cu_xO@TiO_2$ heterostructure with report to the scaffold but used theoretical density functional calculations to prove the proper band alignment between the two materials and thus the effective charge separation. The α-Fe_2O_3/ZnO heterostructured films, prepared by chemical methods, were reported four times more efficient in degrading methylene blue than scaffold α-Fe_2O_3, whereas the effective charge separation and charge transfer were never experimentally proven[45]. Wu *et al.*[46] reported the preparation of NiO/WO_3 p-n heterojunctions by hydrothermal growth followed by dip-coating, achieving 4 times higher photocurrent density than for the scaffold NiO. However, no experimental proof of heterostructure formation was given.
It is worth emphasizing that only a few studies concern NiO/ZNR heterostructures, prepared indeed in a different manner than ours,[47,48] whereas surface and interfacial parameters were rarely considered or correlated with the improved photo-response. Saho *et al.*[47] used electron microscopy combined with XRD and Mott-Schottky to confirm the second material deposition and bonding for NiO/ZNR heterostructures prepared by hydrothermal growth/ spin coating. The photocurrent improvement with the increasing NiO thickness was related to reduced charge transfer resistance and improved light absorption. Cai *et al.*[48] combined hydrothermal growth and immersion to fabricate NiO/ZNR films and relied simply on the observed rectifying I–V behavior for confirming the heterostructure formation.

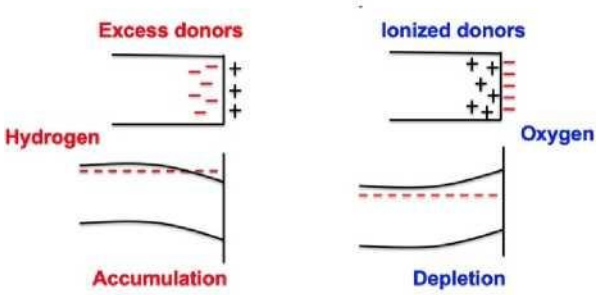

Figure 1. ZnO surface showing the charge distribution, band bending, and electron concentration before and after exposure to atomic hydrogen (left) and oxygen (right). Hydrogen induces electron accumulation (downward band bending), whereas oxygen depletes the surface of electrons (upward band bending).

Only recently Chen *et al.*[49] have proven experimentally the band alignment for NiO/ZNR heterostructures (NiO ultrasonically sprayed onto hydrothermally grown ZNR) and used it to explain the increasing pollutant degradation performance. Nevertheless, no references to surface properties or interface quality were made.

In conclusion, the potential of this heterostructure needs to be further explored as the impact of ZNR surface properties and the NiO thickness are still elusive. Our previous report[50] on NiO/ZNR structures focused on the impact of NiO deposition temperature on cleaned (vacuum annealed) and uncleaned ZNR and highlighted that the establishment of band bending does not guarantee an improvement in pollutant degradation efficiency. It also highlighted that other factors like the scaffold's surface properties, co-catalyst thickness, space charge layer thickness, etc. influence the pollutant degradation efficiency. Thus, in this work, we provide deeper insights into the variation of surface properties of ZNR scaffold (surface chemistry, oxygen vacancy defect fluctuation, and interface quality) as a function of oxygen annealing pressure and their correlation with the interfacial (band bending, conduction and valence band position, Fermi energy) and photo-electrochemical properties (photocurrent, charge transfer resistance, charge carrier density) of the corresponding NiO/ZNR heterostructured films. Also, the role of NiO deposition time on the interface quality was studied. The current

work findings and insights have undoubtedly extended applicability for other metal oxide heterostructures.

Experimental Section

Materials preparation

Firstly, the ZNR scaffold films were hydrothermally grown (growth parameters and nanorods size aspect ratio and structural details already presented in our previous paper[50]) and surface cleaned by annealing in the presence of oxygen at 400°C at different base pressures, 5 and 0.5 Pa. The as-grown ZNR films were noted with Z1, whereas surface-cleaned ZNR were noted with Z2. The letters "L" and "H" were added to Z2 to mark the low (5 Pa) and high (0.5 Pa) vacuum surface cleaning conditions, respectively. Once the surface-cleaning base pressure was optimized, the NiO was deposited at room temperature (RT) by dc sputtering at variable deposition times (20, 40, and 60 s), followed by a post-annealing step at 250 °C for 1 h in presence of 5 sccm oxygen. The deposition was done from a Ni target of 99.99 % purity in the presence of 6% oxygen partial pressure on the optimum surface-cleaned ZNRs. The magnetron power used was 40 W with the substrate placed at 9.5 cm from the target. The letter "N" was added to the sample name whenever a NiO coating was applied and 20s, 40s, and 60s subscripts describe the three deposition times.

Characterization

Transmission electron micrographs were collected at an acceleration voltage of 200 kV (FEI, Tecnai G2TWIN, LaB6 cathode) on films scratched off the substrate and dispersed in ethanol under ultrasonication, then deposited on carbon-coated copper grids. A Varian Cary Eclipse Fluorescence Spectrophotometer equipped with a Xenon flash lamp was used to acquire the PL emission spectra of the ZNR scaffold films (examined area =2 cm ×2 cm). The equipment was operated at an excitation wavelength of 325 nm, while emissions were recorded in the range of 300–850 nm. The electronic, surface and interface characteristics of the scaffold and heterostructured films were investigated using XPS. The measurements were done with the Darmstadt Integrated System for Materials Research (DAISY-MAT) unit, a physical electronics PHI 5700 multi-technique surface analysis, and a thin film deposition system. For the XPS analysis, a monochromatic Al Kα X-Ray source (hν= 1486.6 eV) was used and spectra were recorded at room temperature at a photoelectron take-off angle of 0 degrees (normal emission). The Fermi edge of sputter cleaned Ag standard was used for the binding energy (BE) calibration, before acquiring the binding energies of the respective elements.

Photo-electrochemical Impedance Spectroscopy (PEIS) and linear sweep voltammetry (LSV)

PEIS and LSV analysis were used to investigate the charge transfer resistance, the onset potential, and the photocurrent response. For these measurements, a Xenon lamp (Arc Lamp Source, 450 WXe Ozone Free, F/1 from Newport) was used as a light source, coupled with a KG3 IR filter (Edmund optics), operated at 1 sun. The PEIS was realized in the 800 kHz–200 mHz frequency range, with a signal amplitude of ± 15 mV, whereas the LSV conditions were (the used was 0 to 1.6 V potential window and 20 mV/s scanning rate. Mott-Schottky analysis was carried out in dark for determining the carrier concentration and the flat band potential for the scaffolds obtained at different vacuum chamber pressures. The used potential window was 0.8 to 0.5 V and the frequency domain 100 mHz–200 KHz (comprising 52 steps). The photocatalytic film's corrosion resistance was probed in dark by measuring the Taffel plots at a 10 mV/s scanning rate. For all these electrochemical measurements, a 3-electrode home-made cappuccino cell was used (with quartz glass window for assisting the illumination on photocatalyst surface) which consisted of a counter electrode (Platinum wire), an aqueous Ag/AgCl reference electrode (E *vs.* SHE = 0.204 V), and the thin films as working electrodes. All the measurements were done in a 0.5 M $Na_2SO_4 \cdot 10H_2O$ aqueous solution (pH-6.6) by using a 1 ×1 cm^2 sample area.

Photo-degradation tests

Photo-degradation tests were carried out for the optimized samples by using 20 mL ($1.3 \cdot 10^{-6}$ M) of Rhodamine-B – RhB (Sigma Aldrich, 95 %) solution. The prepared substrates were cut into 1 cm × 1 cm and supported around 0.13 mg of photocatalyst and used in the degradation studies. Initially, the film was kept in dark for 20 min, with

mild stirring, to confirm the absence of any dye degradation processes related for example to pollutant adsorption to the glassware. Samples were then exposed to UV light (4.0 mW/ cm^2) for 180 min and, systematically, 1 mL of aliquot sample was taken at time 0 and every 20 min for UV-visible spectrophotometry.

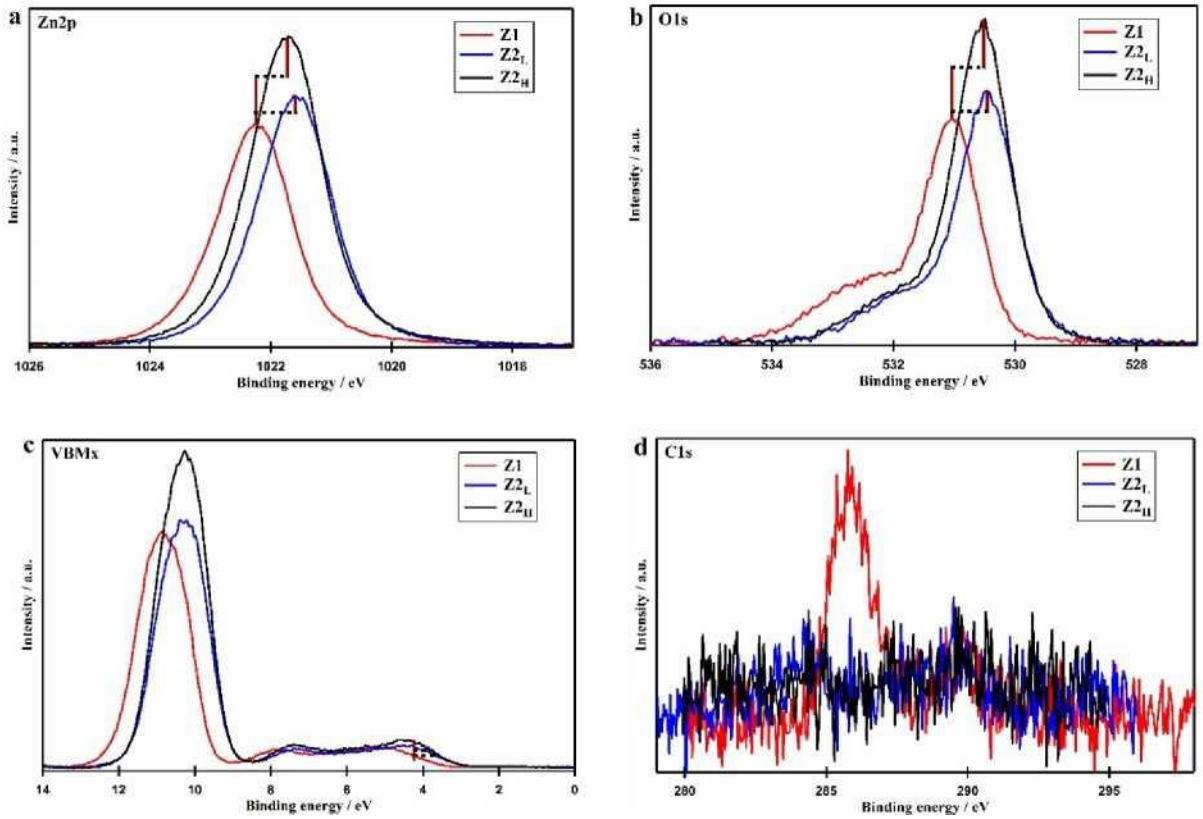

Figure 2. XPS spectra showing the Zn2p (a), O1s (b), VBMx (c), and C1s (d) peaks of Z1, $Z2_L$, and $Z2_H$ scaffold films.

Results and Discussion

Characterization of the scaffold films

ZNR morphology

The SEM characterization detailed in our previous work[50] showed that the scaffold morphology is characterized by densely and randomly packed nanorods of 250–300 nm in length and 50– 60 nm thick, with an average aspect ratio of 5. The (002) preferentially oriented wurtzite phase (JCPDS car no. 79–2205) could be confirmed through XRD[50] in our previous study.

XPS analysis

All the scaffold films were primarily examined by XPS to explore the native surface characteristics and their modification with surface cleaning. The survey scans (not shown in the paper) confirmed that the emissions were only from the respective characteristic elements.

Through low ($Z2_L$) and high ($Z2_H$) pressure scaffolds cleaning, the Zn_{2p} and O_{1s}, core level lines, and the valence band maximum (VBMx) increased in intensity compared to the uncleaned Z1 (Figures 2a to 2c), which confirmed the removal of adsorbates. The C1s emission was not detected either in $Z2_L$ or $Z2_H$ (Figure 2d). Moreover, the Zn_{2p} and O_{1s} core level lines shifted towards lower binding energy after surface cleaning (Figures 2a and 2b and Table 1). The shifts in BE of the Zn_{2p} peak were used to estimate the attained band bending (V_{bb} values shown in Table 1)[51]. The higher vacuum annealed scaffold ($Z2_H$, 0.5 Pa) exhibited a lower band bending compared to the low vacuum one ($Z2_L$, 5 Pa). The

Table 1. Binding energies and FWHM values of the Zn 2p and O 1 s peaks, E_F-VBMx, and V_{bb} values expressed in units of electron volts [eV] and O_L/ O_{Tot} ratio values for Z1, $Z2_L$, and $Z2_H$ scaffold films.

Sample Peak Feature	Z1	Z2L	Z2H
Zn2p	1022.33	1021.57	1021.83
O1s	530.97	530.46	530.67
EF-VBMx	3.47	2.85	3.04
Vbb	–	0.76	0.50
FWHMZn2p	1.54	1.45	1.40
FWHMO1s	1.08	1.06	1.08
OL/OTot	0.60	0.78	0.82

Fermi level to valence band maximum distance (E_F VBM_x) was in the range of 2.85–3.47 eV (Figure 2c, Table 1), typical for an intrinsic n-type character. The E_F-VBM_x shift indicated that E_F was above the conduction (CB) band for the uncleaned Z1 scaffold and lowered below the CB through surface cleaning (Figure 3), indicating a change in the surface doping level. Besides, a narrowing of the Zn_{2p} line was also noticed (FWHM values in Table 1).
The O_{1s} spectra of all the scaffolds (Z1, $Z2_L$, and $Z2_H$) were deconvoluted (after Shirley background processing, using IgorPro), as shown in Figures S1a–c in Supporting Information. The O_{1s} line of cleaned scaffolds ($Z2_L$ and $Z2_H$) could be fitted with two components namely, lattice oxygen-O_L and surface hydroxyls-O_{OH}, centered at 530.5 eV and 531.8 eV, respectively, whereas three contributions were assigned for the uncleaned Z1 (O_L 530.97 eV, O_{OH} 532.1 eV and molecular water, O_{H2O} 532.78 eV[52]). The presence of O_{H2O} in Z1 is typical for an ambiance-exposed sample. The intensity areas of the deconvoluted oxygen peaks were used to calculate O_L/O_{Tot} (O_{Tot} – total peak intensity area) and the lattice oxygen contribution was shown to increase in the order Z1 < $Z2_L$ < $Z2_H$ (Table 1) along with the disappearance of the O_{H2O} peak (Figure S1 in Supporting Information) confirming the removal of the HO-adsorbates.
In general, when the semiconductor surface is in contact with a heated gaseous atmosphere, the resultant layer would be the result of a balance between the adsorption of atoms/molecules from the atmosphere (here, oxygen and H_2O) and the thermal excitation of electrons from the surface of the material.[53] As these effects cannot easily be separated, a homogeneous bulk doping charge for the nanostructured samples is assumed. Oxygen vacancy filling is a process that occurs as a competition between temperature and oxygen partial pressure involved.[30]

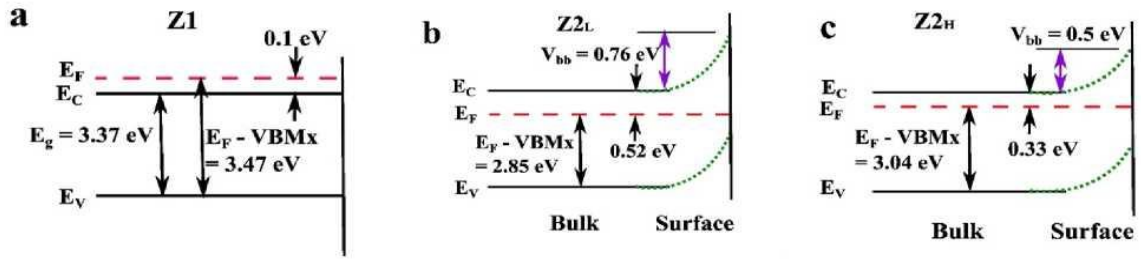

Figure 3. Band energy diagram of (a) the uncleaned Z1, (b) the low $Z2_L$ and (c) high $Z2_H$ vacuum surface cleaned scaffold surfaces.

Under a lower vacuum (5 Pa), oxygen adsorption was favored with a concomitant filling of the oxygen vacancies (equation 1) and electrons depletion at the surface of the ZNR occurred (Figure 1). Because of the surface coverage by oxygen, further adsorbates desorption was hindered explaining the higher HO- content at the surface [Equation (1)].

$$\frac{1}{2}\,O_2\,(gas) + 2e^- + V_O^{\cdot\cdot} \rightleftharpoons O_O^{\times} \qquad (1)$$

In exchange, by annealing in oxygen at a higher vacuum (0.5 Pa) the equilibrium of reaction in Equation (1) was moved to the left favoring oxygen desorption which resulted in e release and the
Fermi level was increased (E_F-VBM_x value of $Z2_H$ higher than that of $Z2_L$, Table 1). Undoubtedly, the chamber vacuum pressure variation affects the ZNR scaffold doping.

Although the electron depletion at the surface of $Z2_L$ was higher than that of $Z2_H$, the latter is expected to have improved interfacial properties as a higher amount of HO- was removed (higher O_L/O_{Tot} ratio, Table 1).

Photoluminescence (PL)

The photoluminescence response of pristine (Z1) and high vacuum surface cleaned ZNR ($Z2_H$) samples highlighted the variation in the oxygen vacancies level with surface cleaning and strengthen our XPS observation on doping level modification.

The deconvoluted PL spectra of Z1 and $Z2_H$ are shown in Figures 4a and b, respectively. Two major peaks situated in the 387–397 nm (narrow) and 450–800 nm (broad) range were observed and attributed to the Near Band-edge Emission (NBE) and the Deep Level Emission (DLE). NBE occurred due to surface recombination, whereas DLE can be attributed to deep trap levels (vacancies) in ZnO. Conventionally, the ZnO PL emissions span within the range of 300–800 nm and are separated into regions as follows: UV (375–395 nm), blue (405–450 nm), green (500–560 nm), orange (600–640 nm) and red (650–750 nm).[32,54,55] Surface excitons (FX),[33,56] Zn vacancies (V_{Zn}), Zn interstitials (Zn_i),[36,57] oxygen vacancies (V_O) and oxygen interstitials (O_i)[58,59] are hiding below the deconvoluted peaks (Figure 4). The narrow NBE peak (UV emission) was the result of free surface excitons but also of shallow-level defects like Zn_i. The broad DLE peak included blue, green, orange, and red emissions. The transition between Zn_i and V_{Zn} levels led to the blue emission, which overlapped with that of trapping O_i species whose contribution lies in the green emission.

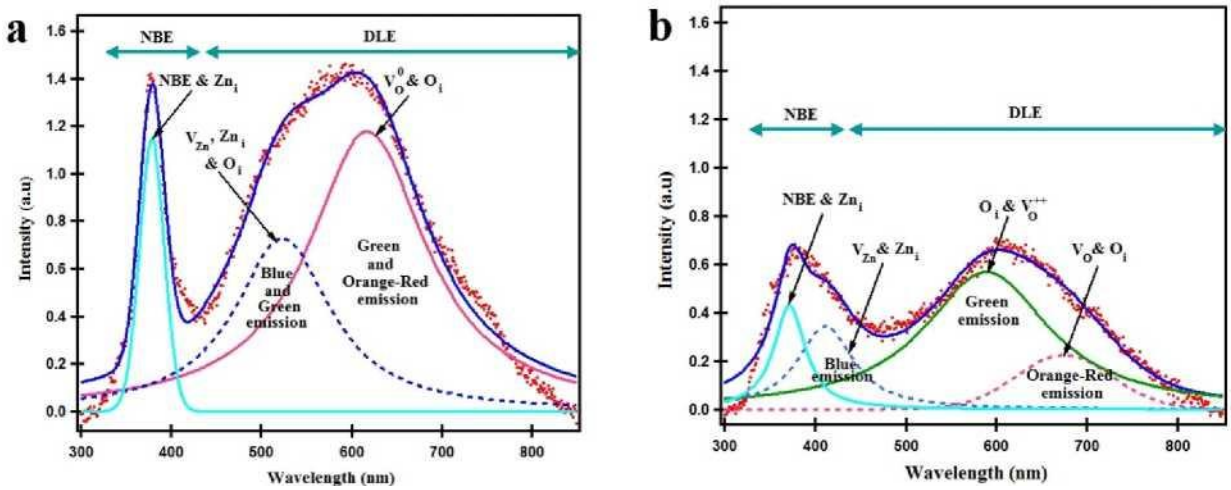

Figure 4. Deconvoluted PL spectra of Z1 (a) and $Z2_H$ (b) scaffold films.

The peak centered at 602 nm indicated the presence of excess electrons as it corresponded to neutral oxygen vacancies (V^o_O),[57–59] which corresponds with XPS studies which showed that the E_F lies above the conduction band minimum and an electron accumulation layer is formed at the surface of Z1. In the case of $Z2_H$, all the contributions previously discussed were identified but with shifted and decreased intensity levels. The loss in intensity suggested that the vacuum surface cleaning in presence of oxygen was efficient in decreasing the number of recombination centers. This is in good agreement with XPS showing a shift of Fermi level position below the CB after cleaning. The NBE peak of $Z2_H$ underwent a blue shift and was slightly broadened as an effect of the vacuum thermal treatment (Figure 4b and Table 2). The I_{NBE}/I_{Total} ratio increased and the I_{DLE}/I_{Total} ratio decreased after cleaning, indicating a reduction in the oxygen vacancy defect concentration as desired for a high-quality interface formation with a second material. The still rather high contribution of the deep-level emission for both ZNR samples could be as a result of HO re-adsorption from the environment during transfer of the sample to the PL instrument.

For the cleaned scaffold ($Z2_H$), the NBE peak exhibits a shoulder (Figure 4b) which was attributed to the Zni and VZn.[33,36,57] Neutral vacancies ionization through cleaning was confirmed through PL analysis as the peak corresponding to V_O reduced in intensity and blue shifted,[31,54] apart from the oxygen vacancy filling effect indicated by XPS analysis.

Mott-Schottky analysis

The donor density (N_D) and the flat band potential (E_{FB}) values for the scaffold films were extracted from the Mott-Schottky plots (Figure 5) and confirmed the change in doping evidenced by XPS. The variation of the double layer capacity (developed at the semiconductor electrolyte interface) as a function of potential is described by the Mott-Schottky equation [Eq. (2)]:[60,61]

$$\frac{1}{C_{SC}^2} = \left(\frac{2}{e\varepsilon_0\varepsilon_r N_D A^2}\right)\left(E - E_{FB} - \frac{KT}{e}\right) \quad (2)$$

where C_{SC} = the capacitance of the space-charge region of the film at potential E, E_{FB} = band potential, N_D = free carrier concentration of the semiconductor, and A = area (~ 0.8 cm^2); e = charge of the electron, ε_0= permittivity of free space, ε_r= relative dielectric constant of ZNR (2.7[62]), k = Boltzmann constant, and T = absolute temperature. Further on, the slope of the linear section (Figure 5) was used to determine the charge carrier concentration (N_D) according to Equation (3). The intersection of the linear part with the x-axis (extrapolating the graph with $C^2 = 0$), gives the flat band potential (E_{FB}).[63] The N_D and E_{FB} values were gathered in Figure 5d [Equation (3)].

$$N_D = \left(\frac{2}{e\varepsilon_0\varepsilon_r A^2 (slope)}\right) \quad 3)$$

As expected, the donor density diminished after surface cleaning,[29] in agreement with the Fermi level lowering below the conduction band. $Z2_L$ was noticed to have a lower carrier density than $Z2_H$ and consequently a wider depletion region. It is the first time that the changes in the surface doping level are simultaneously confirmed by XPS, PL, and Mott-Schottky analysis. To conclude this part, surface cleaning at high vacuum enabled the adsorbates and surface defects removal with important consequences on the ZNR doping level. As follows, only the $Z2_H$ scaffolds were used to build heterostructures with NiO, using various deposition times, and samples were further characterized.

NiO deposition time optimization

Morphology

The TEM images corresponding to NiO-covered ZNR for varying deposition times are shown in Table 3 along with the expected and measured NiO layer thicknesses. For 20 s of deposition, a very thin layer of NiO, 3 nm thick (Table 3) could be observed. Though ZnO and NiO could not be distinguished from the image, the FFT observations allowed the determination of the lattice spacings d = 0.24 nm and d = 0.26 nm, corresponding to NiO (111) and ZnO (002) planes, respectively. Deposition at 40 s resulted in thicker layers, 6–7 nm. For 60 s of deposition time, the growth of bigger particles branching out from the ZNR surface could be observed.

XPS analysis

The Zn_{2p}, $Ni_{2p,}$ and O_{1s} core levels and valence band maximum evolution as a function of the NiO deposition time are shown in Figure 6. The BE of Zn_{2p}, $O_{1s,}$ and VBM_x were all shifted towards lower values (Figure 6 and Table 4) due to NiO deposition and a consequent change in the chemical environment. No clear trend relating the change in intensities with the NiO deposition time could be distinguished. However, BE shifts were observed and used to extract information about the influence of deposition time on band bending.

The Zn_{2p} emission line was noticed to be centered in the range of 1020.94–1021.04 eV (Figure 6), with little differences between the various coating times. Similarly, negligible shifts in the Ni_{2p} main, shoulder, and Ni_{Sat} peaks could be observed (Figure 6). Moreover, changes in the O_{1s} and Ni_{2p} core level lines as a function of deposition time were only noticed for the $Z2_HN_{40s}$. For this sample, an increase in the O_{1s} shoulder indicated a surface richer in hydroxyls (Figure 6), and a mild shift in Ni_{sat} was noticed, compared to its 20 s and 60 s counterparts. The FWHM of O_{1s} was observed to gradually decrease from lower to higher deposition times and this could be ascribed to oxygen sharing between Zn and Ni. Likewise, the broadening of the Zn_{2p} peak for the 40 s sample suggested a more intimate bonding between the two materials.

Finally, the shifts in BE of Zn_{2p} were used to estimate the attained band bending at the interface of each heterostructure, with the help of Equation (4) below:[64]

$$V_{bb} = BE_{Zn2p}(i) - BE_{Zn2p}(f) \quad (4)$$

where (i) and (f) refer to the BE values of the Zn_{2p} peak obtained at the initial and final steps, respectively. The values are given in Table 4 ranging between 1.33 and 1.39 eV. Interestingly, the Fermi level was the lowest for the 60 s sample (lower E_F-VBM_x value in Table 4) and we believe that owing to the particle-grafted morphology of the NiO the post-annealing had a cleaning effect on the ZNR surface.

Table 2. NBE and DLE peak maxima position/shift direction, the FWHM of the NBE peak, and the I_{NBE}/I_{Total} and I_{DLE}/I_{Total} intensity ratios.[a]

Sample Code	NBEmax [nm]/Shift	DLEmax [nm]/Shift	FWHMNBE [nm] [a]	INBE/ITotal [a]	IDLE/ITotal
Z1	371/–	602/–	38	0.18	0.82
Z2H	367/Blue	570/Blue	40	0.21	0.78

[a] Intensity ratios calculated based on the PL spectra shown in Figure 4 The area under the deconvoluted NBE (cyan colored line) and DLE peaks (blue, pink,green colored lines) was integrated and reported to the total intensity obtained by integrating the area below the blue envelope - peak deconvolution was

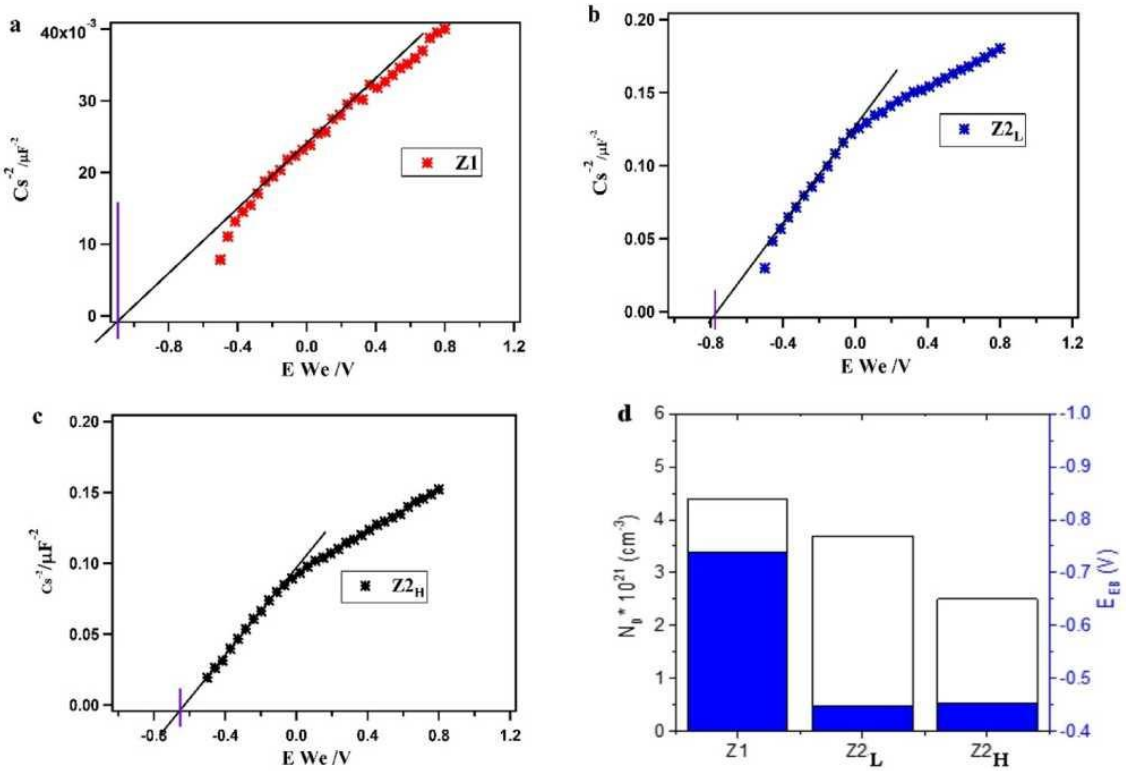

Figure 5. The Mott–Schottky plots of the Z1 (a), $Z2_L$ (b), and $Z2_H$ (c) scaffold films, measured in 0.5 M $Na_2SO_4 \cdot 10H_2O$ aqueous solution, and the N_D and E_{FB} values (d).

Table 3. TEM images [a] and data for the NiO-coated ZNR as a function of deposition time and corresponding expected and measured NiO layer thicknesses.

Deposition time	20 s	40 s	60 s
Nanorods morphology		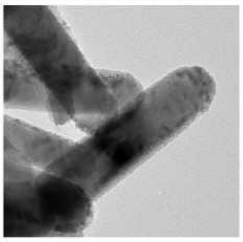	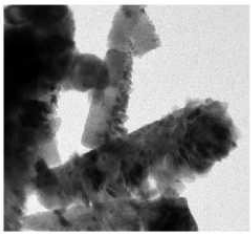
Expected NiO layer thickness [nm] based on deposition rate	3–5	7–10	12–15
Measured layer thickness from TEM [nm]	3	6–7	No layer but particles

[a] The scale in the TEM images represents 50 nm.

Table 4. Sample names and their respective binding energies of Zn2p, O1s, Ni^{2+}, and Ni_{sat} peaks, band bending and FWHM values of Z2p and O1s peak, for all heterostructured films; all are expressed in units of electron volts [eV].

XPS spectra (in eV)	Z2H	Z2HN 20 s	40 s	60 s
Zn2p	1021.83	1020.95	1021.04	1020.94
O1s	530.67	529.51	529.43	529.47
Ni^{2+}	–	853.96	853.82	853.91
Nisat	–	861.14	861.00	861.12
Ef-VBMx	3.04	0.63	0.66	0.59
V_{bb}[a]	0.50	1.38	1.33	1.39
FWHMZn2p	1.4	1.46	1.62	1.47
FWHMO1s	1.08	1.12	1.09	1.06

[a] 0.50 eV was added to the V_{bb} values of all $Z2_H$ heterostructures, with respect to the shift of the Zn 2p line for the $Z2_H$ scaffold with the reference material, Z1 scaffold.

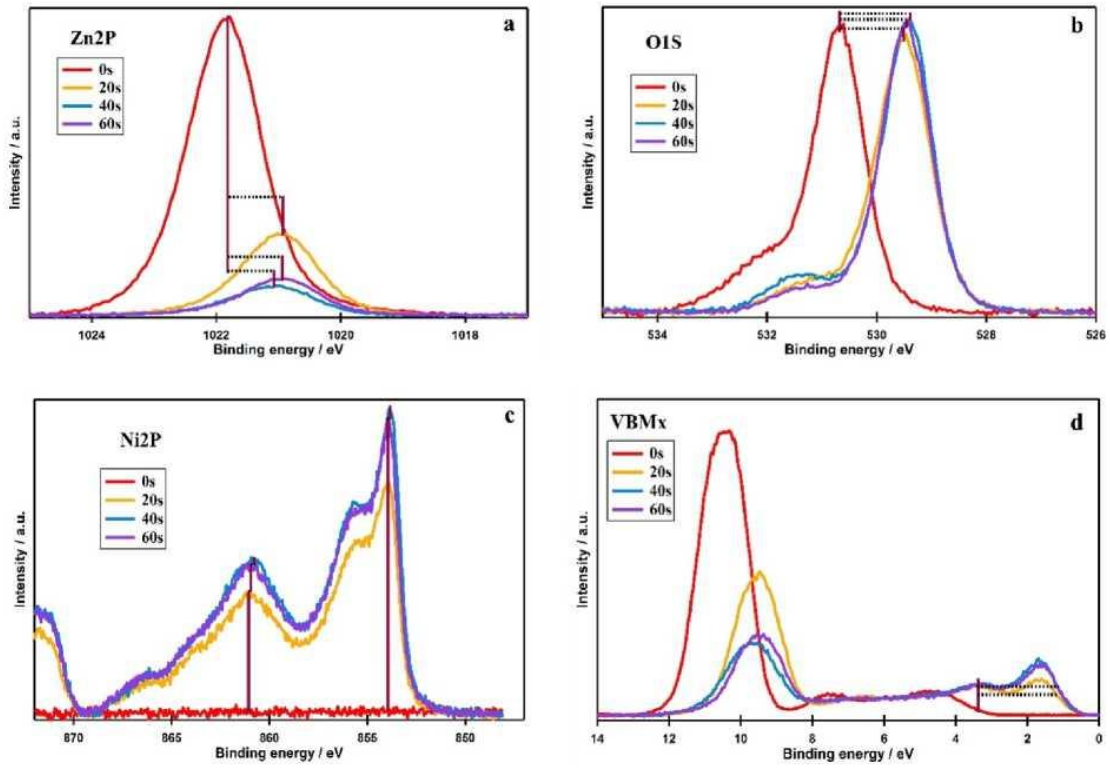

Figure 6. XPS spectra showing the Zn 2p (a), O1s (b), Ni 2p (c), and VBMx (d) peaks of the $Z2_H$ compared with NiO/ZNR heterostructures as a function of the various NiO deposition times.

Photoluminescence

Furthermore, to understand the effect of NiO deposition time on the interface quality, the photoluminescence spectra of $Z2_H$ were compared with its respective heterostructures for which the NiO deposition time was varied (Figure 7). For further interpretation of the contribution of surface excitons and defects in charge carrier recombination, the intensity ratios I_{NBE}/I_{Total} and I_{DLE}/I_{Total} were determined (after deconvolution) and reported in Table 5.

After NiO deposition, the intensity of the deep-level emission decreased (Figure 7) but still exceeded the near band edge

emission (Table 5), suggesting that despite the improved charge separation non-radiative recombination across the NiO layer might have occurred. For the 40 s deposition times, the NBE contribution exceeds that of DLE indicating reduced charge recombination and the formation of a good-quality interface between the two materials. The DLE contribution raises for longer deposition times indicating increased charge recombination which is detrimental to photocatalytic processes. The NBE peaks of almost all the heterostructures were red-shifted (Table 5) signifying an enhancement in the quantum confinement effect, because of nanoscale NiO covering.

So, we conclude that depositing the NiO for the 40 s on a high vacuum-cleaned ZNR scaffold followed by post-annealing leads to conformal nanorods covering (TEM) and a high-quality interface formation as (1) an intimate bonding and consequent band bending could be proven through XPS and (2) effective charge separation along with reduced charge recombination were demonstrated through PL analysis.

(Photo)electrochemical analysis

The current-voltage (*I*–*V*) curves were recorded in light for the $Z2_HN_{40s}$ heterostructure with respect to the $Z2_H$ scaffold, as represented in Figure 8a. The following features were extracted from the I–V plots (values shown in Table 6): (i) the onset potential (V_{OP}) (ii) the photocurrent produced at the water-splitting voltage 1.026 V, $I_{1.026V}$ (vs. Ag/AgCl) and (iii) the maximum photocurrent density that can be attained at potentials more anodic than 1.026 V, I_{max}. The determination of the onset potential was done by extrapolating the linear portion of the I–V curve to the x-axis.[65]

Table 5. Sample codes and corresponding information extracted based on the PL spectra in Figure 7.

Sample code	NiO deposition time	NBE Peak maximum position [nm] / shift	FWHM of NBE [nm]	INBE/ ITotal [a]	IDLE/ ITotal [a]
Z2H	–	375.00	40.00	0.21	0.78
	20 s	384.23/Red	34.60	0.14	0.32
Z2HN	40 s	381.00/Red	48.17	0.08	0.04
	60 s	383.50/Red	36.20	0.05	0.13

[a] Intensity ratios calculated based on the PL spectra shown in Figure 7 . Peak deconvolution was realized using the data analysis software IgorPro as already exemplified in Figure 4 and ratios were calculated as described in the caption of Table 2.

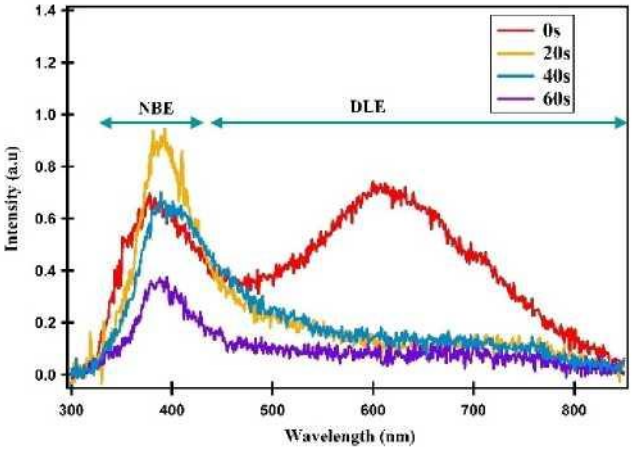

Figure 7. Photoluminescence spectra of $Z2_H$ (surface cleaned at higher vacuum) and its heterostructures with NiO deposited at different deposition times.

Theoretically, the E_{FB} is the potential at which photocurrent will arise, but this is never the case because of surface recombination or accumulation of electrons (if p-type) / holes (if n-type) at the surface, as a result of poor charge transfer kinetics.[66] Therefore, the V_{OP} (Table 6) is higher than E_{FB} (Table 6) but the trend was maintained.

As previously demonstrated through XPS, the surface of the uncleaned scaffold was rich in electrons (E_F above the CB, accumulation regime) which were easily transferred to the electrolyte, explaining the higher photocurrent values of the uncleaned scaffold (Z1). Whereas for the high vacuum cleaned scaffold ($Z2_H$) the electrons are forced to overcome a barrier before being transferred to the electrolyte, due to the presence of a depletion regime, thus justifying the lower photocurrent (Table 6). Our conclusions do not account for the eventual band-bending evolution when the heterostructure comes in contact with the electrolyte, but we assume (considering our recent tests) that this contribution is minor. Aqueous environment exposure tests are in progress to elucidate this aspect.

The higher photocurrent indicators ($I_{1.026V}$ and I_{tot}) for the $Z2_HN_{40s}$ heterostructure versus the $Z2_H$ scaffold suggest improved charge transfer kinetics and reduced surface charge recombination as indicated by XPS and PL analysis. In addition, the $Z2_HN_{40s}$ heterostructure was more corrosion resistant than the scaffold as observed from the Taffel plots registered in the dark (Figure 8b), where the corrosion potential of the heterostructure was shifted to the right with report to the scaffold.

Photo-electrochemical impedance spectra (EIS) were recorded for the same two samples and Nyquist plots are shown in Figure 9. The $Z2_H$ Nyquist plot was fitted with an equivalent circuit composed of five elements [R_s + $RCT_1$1 | Q1 + R_{CT2} | | Q2] - where + and || represents series and parallel connection respectively. The $Z2HN_{40s}$ was fitted with a circuit comprising six elements [R_s + R_{CT1} | | Q1 + R_{CT2} | | Q2 + Q3], due to obvious diffusion process. The electrical circuit and the fitting approach are detailed in Figure S2 in the supporting information. Here, R_S stands for the contacts and electrolyte resistance, R_{CT1} || Q1 is attributed to the charge transfer impedance through the catalysts here including charge travel through bulk and FTO/photocatalysts interface, whereas R_{CT2} | | Q2 corresponds to the charge transfer resistance and capacity of the double layer formed at the photocatalyst/electrolyte interface. In the case of $Z2_HN_{40s,}$ the Q3 was used to define the diffusion-like behavior at low frequencies. The values of circuit elements obtained through fitting were gathered in Table 7.

The slight changes in Rs were due to layer etching for obtaining a direct contact on FTO. This process is hardly reproducible leaving the surface more or less resistive. We can notice that the charge transfer through the photocatalyst (R_{CT1}) was slightly decreased with the deposition of NiO which might be related to an improved contact between the electrolyte and the ZNRs. The straightforward information obtained from EIS is that the heterostructure/electrolyte charge transfer resistance (R_{CT2}) was markedly reduced. Even more, in the case of the $Z2_HN_{40s}$ heterostructure the charge accumulation is readily observed (Figure 9b).

The maximization photocurrent density of the $Z2_HN_{40s}$ heterostructure with report to its scaffold was correlated to the effective bonding between the two materials (as proven by XPS) but also to the mitigation of the interface charge recombination as demonstrated through EIS (lower charge transfer resistance) and PL studies. This

demonstration of enhanced photoelectrochemical performance and its correlation with the material properties stands out from the other reports which simply empirically attribute the increase in performance to effective charge separation.[44–48] It is important to note that the interfacial properties of the NiO/ZNR heterostructure were realized in-situ (PVD deposition chamber), with no influence from environmental pollution.

Table 6. Open potential voltage (V_{OP}), the photocurrent density at 1.026 V vs. Ag/AgCl ($J_{1.026V}$) and the maximum photocurrent density (Jmax) extracted from Figure 8a and corrosion potential (E_{corr}) and current (J_{corr}) for the bare FTO, and $Z2_H$ and $Z2_HN_{40s}$ covered FTO derived from Figure 8b.

Sample	VOP [V]	J1.026V [mA/ cm^2]	Jmax [mA/ cm^2]	Ecorr [V vs Ag/ AgCl]	Jcorr [A cm^{-2}]
FTO	1.37	0.64e ^{3}	8.01e ^{3}	0.09	6.81
Z2H/FTO	1.22	0.047	4.64	0.17	5.18
Z2HN40s/ FTO	1.19	0.075	6.60	0.154	5.34

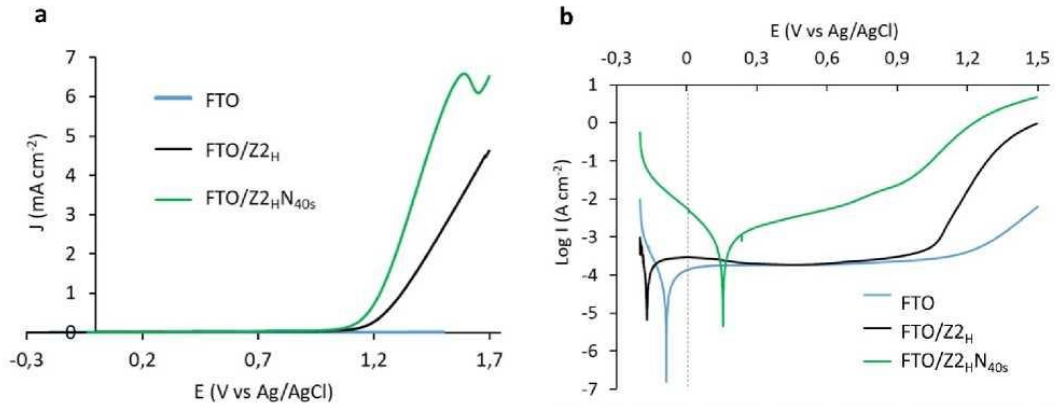

Figure 8. *I–V* plots registered in light (a) and Taffel plots registered in the dark (b) for the $Z2_H$ and $Z2_HN_{40s}$ thin films on FTO versus the bare substrate.

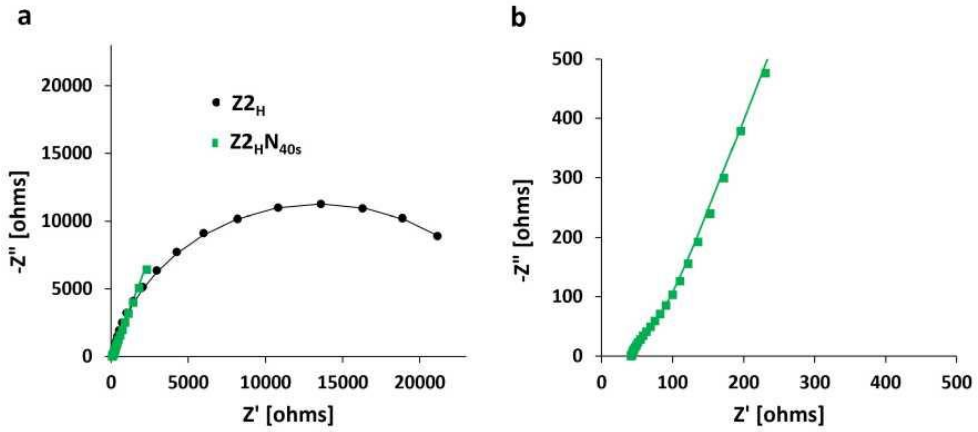

Figure 9. (a) Nyquist plot for the $Z2_H$ scaffold and its heterostructures $Z2_HN_{40s}$ and (b) zoomed view of the $Z2_HN_{40s}$. In this figure, the continuous line represents the fitted curve.

Table 7. Values of the R_S, R_{CT1}, and R_{CT2} obtained through fitting the Nyquist plots in Figure 9 with the circuit described in Figure S2 in the Supporting Information.

Sample	RS [Ω]	RCT1 [Ω]	RCT2 [Ω]
Z2H	70.0	36.2	26863
Z2HN40s	36.6	5	30

Pollutant degradation

The photocatalysts $Z2_H$ and $Z2_HN_{40s}$ were checked for their ability to degrade the pollutant Rhodamine B. While $Z2_H$ already shown an improvement with report to uncleaned ZNR, $Z2_HN_{40s}$ was found here to have a modest improvement in performance compared to its scaffold. $Z2_HN_{40s}$ showed a degradation efficiency of 69% at low light irradiance (4 mW/cm^2) with a degradation speed of 6×10^{-3} min^{-1} as compared to 64% degradation at a speed of 5.7×10^{-3} min^{-1} for $Z2_H$. Though interfacial defects have been effectively decreased for 40 s NiO deposition, the degradation results indicate that charge recombination across the NiO layer[37] might have occurred. Comparing with the literature is not straightforward as different conditions are used each time in terms of pollutant type and concentration, photodegradation time, light source, and irradiance (see Table 8). In addition, the ZnO-NiO immobilized photocatalyst was very less studied. Compared to a previous study reporting the same type heterostructure[49] as ours, we obtain similar photodegradation efficiencies (70 %) for a pollutant that is much harder to degrade, the RhB. Again, higher efficiencies are reported for ZnO/CuO heterostructured films built on ZNR scaffold[67,68] but also for TiO_2/In_2O_3 films built on TiO_2 nanotube scaffold[69] for the standard MB dye. Incredibly high efficiency is reported for the degradation of RhB for physically deposited CuO/ TiO_2 flat films but details on the irradiance level are not given.[70] The markedly high efficiency obtained for the degradation of MO and RhB by using ZNR-based heterostructures with either $CuInS_2$ or TiO_2 as co-catalyst are obtained for much higher irradiance levels than the irradiance we used.[71,72] We note that much lower efficiencies than ours (40% as opposed to 69%) were obtained for ZnO and CuO_2-covered TiO_2 nanotube[73] and nanorod[74] films, respectively.

Table 8. Comparison of the photocatalytic performance of the NiO/ZNR heterostructured films reported in this work with other similar photocatalytic systems.

Substrate	Scaffold/ deposition method	2nd material/ deposition method	Tested pollutant[a]	Pollutant concentration [mg/L]	Irradiance [mW/ cm^2]	Photocatalytic efficiency	Ref.
Glass	ZnO nanorods/hydrother- mal	NiO/ultrasonic spray	MB	10.0	Not reported	70%in3h	49
Quartz	ZnO nanorods/hydrother- mal	CuO/hydrothermal	MB	3.2	Not reported	85 % in 3 h	67
Quartz	ZnO nanorods/hydrother- mal	CuO/photochemical	MB	5.0	6	95 % in 3 h	68
Ti foil	TiO_2 nanotubes/ anodization	In_2O_3/anodization	MB	n.a.	visible	96%in 3 h	69
ITO glass	CuO/sputtering	TiO_2/sputtering	RhB	5.0	Not reported	93 % in 2 h	70
FTO glass	ZnO nanorods/hydrother- mal	$CuInS_2$/electrophoresis	MO	20.0	50	85 % in 3 h	71
FTO glass	ZnO:I nanorods/ chemical growth	TiO_2/Soaking	RhB	2.4	100	97% in 6 h	72
Ti foil	TiO_2 nanotubes/ anodization	ZnO/Immersion	MO	32.7	10.5	40% in 2 h	73
FTO glass	TiO_2 nanorods/ hydrothermal	CuO_2/hydrothermal	RhB	4.8	Not reported	40% in 5 h	74
FTO glass	ZnO nanorods/hydrother- mal	NiO sputtering	RhB	0.6	4	69%in 3 h	This work

[a] MO=methyl orange, RhB= rhodamin B, MB = methylene blue, O II = orange II.

Conclusion

We have studied the impact of ZNR scaffold surface properties (adsorbates, defects) and second material thickness on the quality of the formed NiO/ZNR heterostructure and its photochemical and photocatalytic activity. The vacuum level during the scaffold surface cleaning and the NiO deposition times were the varied parameters. Adsorbates and oxygen vacancies were more effectively removed when using high vacuum (0.5 Pa)

surface cleaning as confirmed through in-situ XPS and PL analysis. There were evident consequences on the doping level of ZNR, that is, the Fermi level was lowered indicating a change in the scaffold doping level. Further on, the effect of NiO deposition time on the high vacuum (0.5 Pa) surface- cleaned ZNR was studied. XPS and PL investigations showed an improved interface quality and reduced charge recombination for the ZNR-based heterostructure with the 40 s deposited NiO as opposed to shorter and longer deposition times.

Our structure-property findings of optimized heterostructure and corresponding scaffold were in agreement with the photocurrent and charge transfer resistance results. A maximized photocurrent and minimized charge transfer resistance (photo-electrochemical and impedance spectroscopy) were obtained and correlated to an effective bonding between the two materials (XPS) and the reduced deep-level recombination (PL).

Therefore, our study emphasizes the need for a deeper comprehension of the structure-property-performance relationship for designing and enhancing the photocatalytic performance of metal oxide–based heterostructured materials. Though our study focuses on NiO/ZNR heterostructures, these principles could be extended to other metal oxide-based photo- catalytic systems.

Acknowledgments
This work was carried out in the framework of EJD-FunMat (European Joint Doctorate for Multifunctional Materials) and has received funding from the European Union's Horizon 2020 research and innovation programme under the Marie Sklodowska Curie Grant Agreement No. 641640.

Conflict of Interest
The authors declare no conflict of interest.

Data Availability Statement
The data that support the findings of this study are available on request from the corresponding author. The data are not publicly available due to privacy or ethical restrictions.

References

[1] S. Choudhary, S. Upadhyaya, P. Kumara, N. Singha, V. R. Satsangi, R. Shrivastava, S. Dassa, *Int. J. Hydrogen Energy* **2012**, *37*, 18713–18730.
[2] J. Joy, J. Mathew, S. C. Mathew, *Int. J. Hydrogen Energy* **2018**, *43*, 4804– 4817.
[3] A. Fujishima, K. Honda, *Nature* **1972**, *238*, 37–38.
[4] U. Diebold, S. Li, M. Schmid, *Annu. Rev. Phys. Chem.* **2010**, *61*, 129–148.
[5] R. Dittmann in *Epitaxial Growth of Complex Metal Oxides*, (Eds.: G. Koster, M. Huijben, G.Rijnders) Elsevier Ltd, **2015**, pp. 231–261.
[6] S. Bai, J. Jiang, Q. Zhang, Y. Xiong, *Chem. Soc. Rev.* **2015**, *44*, 2893–2939.
[7] S. Bai, W. Jiang, Z. Li, Y. Xiong, *ChemNanoMat.* **2015**, *1*, 223–239.
[8] P. Gorai, E. G. Seebauer, E. Ertekin, *J. Chem. Phys.* **2016**, *144*, 184708.
[9] L. Lin, J. Liu, J. Lv, S. Shen, X. Wu, D. Wu, Y. Qu, W. Zheng, F. Lai, *J. Alloys Compd.* **2017**, *695*, 1523–1527.
[10] F. Kayaci, S. Vempati, I. Donmez, N. Biyikli, T. Uyar, *Nanoscale* **2014**, *6*, 10224–10234.
[11] D. R. Miller, S.A. Akbar, P. A. Morris, *Sens. Actuators B* **2014**, *204*, 250– 272.
[12] T. Jafari, E. Moharreri, A. S. Amin, R. Miao, W. Song, S. L. Suib, *Molecules* **2016**, *21*, 900.
[13] J. Yan, G. Wu, N. Guan, L. Li, Z. Li, X. Cao, *Phys. Chem. Chem. Phys.* **2013**, *15*, 10978–10988.
[14] D. K. Muthee, B. F. Dejene, *Heliyon* **2021**, *7*, e07269.
[15] D. Wojcieszak, D. Kaczmarek, J. Domaradzki, M. Mazur, *Int. J. Photoenergy* **2013**, 526140.
[16] W. Ouyang, F. Teng Jr., H. He, X. Fang, *Adv. Funct. Mater.* **2019**, *29*, 1807672.
[17] A. K. Ganguli, G. B. Kunde, W. Raza, S. Kumar, P. Yadav, *Molecules* **2022**, *27*, 7778.
[18] S. Liu, C. Han, Z.-R. Tang, Y.-J. Xu, *Mater. Horiz.* **2016**, *3*, 259–364.
[19] K. Manjunath, L. Sagar, R. Yadav, T. Jayalakshmi, V. Reddy, H. Rajanaika, G. Nagaraju, *J. Mater. Res. Technol.* **2018**, *7*, 7–13.
[20] Q.-E. Zhao, W. Wen, Y. Xia, J.-M. Wu, *Thin Solid Films* **2018**, *648*, 103– 107.
[21] S. S. Warule, N. S. Chaudhari, B. B. Kale, A. M. Mahindra, *CrystEngComm.* **2009**, *11*, 2776–2783.

[22] Y.-K. Peng, S. C. Edman Tsang, *Nano Today* **2018**, *18*, 15–34.
[23] Y. Mao, Y. Li, Y. Zou, X. Shen, L. Zhu, G. Liao, *Ceram. Int.* **2019**, *45*, 1724– 1729.
[24] Y. Chen, L. Zhang, L. Ning, C. Zhang, H. Zhao, B. Liu, H. Yang, *Chem. Eng. J.* **2015**, *264*, 557–564.
[25] E. S. Jang, J.-H. Won, S.-J. Hwang, J.-H. Choy, *Adv. Mater.* **2006**, *18*, 3309–3312.
[26] C. Klingshirn, *Phys. Status Solidi B.* **2007**, *244*, 3027–3073.
[27] L.J. Brillson, Y. Lu, *J. Appl. Phys.* **2011**, *109*, 121301–121333.
[28] J. Rodrigues, T. Holz, R. Fath Allah, D. Gonzalez, T. Ben, Maria R. Correia, T. Monteiro, F. M. Costa, *Sci. Rep.* **2015**, *5*, 10783.
[29] Y. Tu, S. Chen, X. Li, J. Gorbaciova, W. P. Gillin, S. Krause, J. Briscoe, *J. Mater. Chem. C* **2018**, *6*, 1815–1821.
[30] C. Drouilly, J.-M. Krafft, F. Averseng, S. Casale, D. Bazer-Bachi, C. Chizallet, V. Lecocq, H. Vezin, H. Lauron-Pernot, G. Costentin, *J. Phys. Chem. C* **2012**, *116*, 21297–21307.
[31] A. R. Gheisi, C. Neygandhi, A. K. Sternig, E. Carrasco, H. Marbach, D. Thomele, O. Diwald, *Phys. Chem. Chem. Phys.* **2014**, *16*, 23922–23929.
[32] G. Saito, Y. Nakasugi, T. Yamashita, T. Akiyama, *Appl. Surf. Sci.* **2014**, *290*, 419–424.
[33] B. Ha, H. Ham, C.J. Lee, *J. Phys. Chem. Solids* **2008**, *69*, 2453–2456.
[34] Y.G. Wang, S. P. Lau, X. H. Zhang, H. H. Hng, H.W. Lee, S. F. Yu, B. K. Tay, *J. Cryst. Growth* **2003**, *259*, 335–342.
[35] M. E. Manríquez, L. E. Noreña, J. A. Wang, L. Chen, J. Salmones, J. González-García, C. Reza, F. Tzompantzi, J. G. Hernández Cortez, L. Ye, H. Xie, *Int. J. Photoenergy* **2018**, *7605306*, 7673–7681.
[36] B. Sarma, S. K. Deb, B. K. Sarma, *J. Phys. Conf. Ser.* **2016**, *765*, 012023.
[37] G. R. Li, T. Hu, G. L. Pan, T. Y. Yan, X. P. Gao, H. Y. Zhu, *J. Phys. Chem. C* **2008**, *112*, 11859–11864.
[38] M. Wang, F. Ren, J. Zhou, G. Cai, L. Cai, Y. Hu, D. Wang, Y. Liu, L. Guo, S. Shen, *Sci. Rep.* **2015**, *5*, 12925.
[39] D. Ma, J.-W. Shi, Y. Zou, Z. Fan, X. Ji, C. Niu, *ACS Appl. Mater. Interfaces* **2017**, *9*, 25377–25386.
[40] J. Li, F. Zhao, L. Zhang, M. Zhang, H. Jiang, S. Lia, J. Li, *RSC Adv.* **2015**, *5*, 67610–67616.
[41] F. Tian, Y. Liu, *Scr. Mater.* **2013**, *69*, 417–419.
[42] T. Jiang, X. Qin, Y. Sun, M. Yu, *RSC Adv.* **2015**, *5*, 65595–65599.
[43] H. Salari, M. J. Sadeghinia, *J. Photochem. Photobiol. A* **2019**, *376*, 279– 287.
[44] Y. Zeng, J. Xue, M. He, C. Li, W. Zhu, S. Li, *Electrochim. Acta* **2021**, *367*, 137426.
[45] J. A. Joseph, S. B. Nair, S. S. John, S. Shaji, R. Philip, *Semicond. Sci. Technol.* **2021**, *36*, 095007, 10.1088/1361-6641/ac07c9.
[46] P. Wu, Z. Liu, D. Chen, M. Zhou, J. Wei, *Appl. Surf. Sci.* **2018**, *440*, 1101– 1106.
[47] P. Sahoo, A. Sharma, S. Padhan, R. Thangavel, *Int. J. Hydrogen Energy* **2021**, *46*, 36176–36188.
[48] J. Cai, L. Ruoping, C. Jianrui, J. Liu, J. Han, M. Huang, *Phys. E* **2022**, *135*, 114974.
[49] Z. Chen, T. Dedova, N. Spalatu, N. Maticiuc, M. Rusu, A. Katerski, I. O. Acik, T. Unold, M. Krunks, *Colloids Surf. A* **2022**, *648*, 129366.
[50] S. Periyannan, L. Manceriu, N. D. Nguyen, A. Klein, W. Jaegermann, P. Colson, C. Henrist, R. Cloots, *Catal. Lett.* **2019**, *149*, 1813–1824.
[51] Y. Gassenbauer, A. Wachaua, A. Klein, *Phys. Chem. Chem. Phys.* **2009**, *11*, 3049–3054.
[52] L. Manceriu, A. Maho, C. Labrugere, E. Tixhon, A. Schrijnemakers, A. Rougier, P. Colson, R. Cloots, *ACS Omega* **2020**, *5*, 14999–15006.
[53] P. C. Smith, B. Hu, N. D. Ruzic, *J. Vac. Sci. Technol. A* **1994**, *12*, 2692.
[54] S. Vempati, J. Mitra, P. Dawson, *Nanoscale Res. Lett.* **2012**, *7*, 470.
[55] A. B. Djurišić, Y. H. Leung, K. H. Tamet, *Appl. Phys. Lett.* **2006**, *88*, 103107.
[56] A. Echresh, C. O. Chey, M. Z. Shoushtari, V. Khranovskyy, O. Nura, M. Willander, *J. Alloys Compd.* **2015**, *632*, 165–171.
[57] M. Kakazey, M. Vlasova, E. A. Juarez-Arellano, T. Torchynska, V. A. Basiuk, *RSC Adv.* **2016**, *6*, 58709–58722.
[58] H. B. Lee, R. Ginting, S. Tan, et al., *Sci. Rep.* **2016**, *6*, 32645.
[59] Q. Zhu, X. Changsheng, L. Huayao, C. Yang, S. Zhang, D. Zenga, *J. Mater. Chem. C* **2014**, *2*, 4566–4580.
[60] C. F. Windisch, G. J. Exarhos, C. F. Windisch, G. J. Exarhos, *J. Vac. Sci. Technol. A* **2000**, *18*, 1677–1680.
[61] L. G. Arriaga, A. M. Fernã, *Int. J. Hydrogen Energy* **2002**, *27*, 27–31.
[62] Y. Yang, W. Guo, X. Wang, Z. Wang, J. Qi, *Nano Lett.* **2012**, *12*, 1919– 1922.
[63] A. W. Bott, *Curr. Sep.* **1998**, *3*, 87–91.
[64] J. C. Hellmann, S. D. Tilley, M. Graetzel, J. Morasch, J. Deuermeier, W. Jaegermann, A. Klein, *ACS Appl. Mater. Interfaces* **2016**, *6*, 21824–21831.
[65] D. K. Bora, A. Braun, *RSC Adv.* **2014**, *4*, 23562–23570.
[66] S. Bai, Y. Xiong, *Chem. Commun.* **2015**, *51*, 10261–10271.
[67] J.-H. Huang, J.-X.g Chen, Y.-F. Tu, Y. Tian, D. Zhou, G. Zheng, J.-P. Sang, Q.-M. Fu, *Mater. Res. Express* **2019**, *6*, 015035.
[68] W. Gao, Z. Li, M. Peng, F. Han, Z. Wei, Z. Yang, Z. Jiang, *Langmuir* **2021**, *37*, 7890–7906.
[69] K. A. John, J. A. Joseph, S. Babu, V. K. Shinoj, S. K. Remillard, S. Shaji, R. R. Philip, *Phys. Status Solidi B.* **2021**, *258*, 2000441.
[70] B. Hao, J. Guo, L. Zhang, H. Ma, *J. Alloys Compd.* **2022**, *903*, 163851.

[71] W. Que, X. Zhang, Y. Xing, X. Yin, Y. Du, *J. Hazard. Mater.* **2016**, *317*, 430–439.
[72] T. Tsuzuki, B. Tang, X. Hou, L. Sun, X. Wang, *ACS Appl. Mater. Interfaces* **2015**, *7 (11)*, 6093–6101.
[73] K. Zhang, X. Wang, D. Zhang, Y. Li, H. Su, H. Zhang, Z. Zhong, *RSC Adv.* **2018**, *8*, 8064–8070.
[74] S. Wannapop, A. Somdee, *Thin Solid Films* **2022**, *747*, 139144.